Supporting Information

A Dielectric-Gradient Composite Gel Polymer Electrolyte Synergistically Enhances Ion-Transport and Interfaces for High-Voltage Lithium-Metal Batteries

Weitong Yang,[a] Panlong Wang,[a] Guofu Zhang,[b] Xinhang Liu,[a] Xueping Gao[a] and Guoran Li[a]*

[a]Institute of New Energy Material Chemistry, School of Materials Science and Engineering, Nankai University, Tianjin 300350, China

[b]Cangzhou Zhongfu New Energy Materials Co., Ltd, Cangzhou 061754, China

*Corresponding Authors: guoranli@nankai.edu.cn

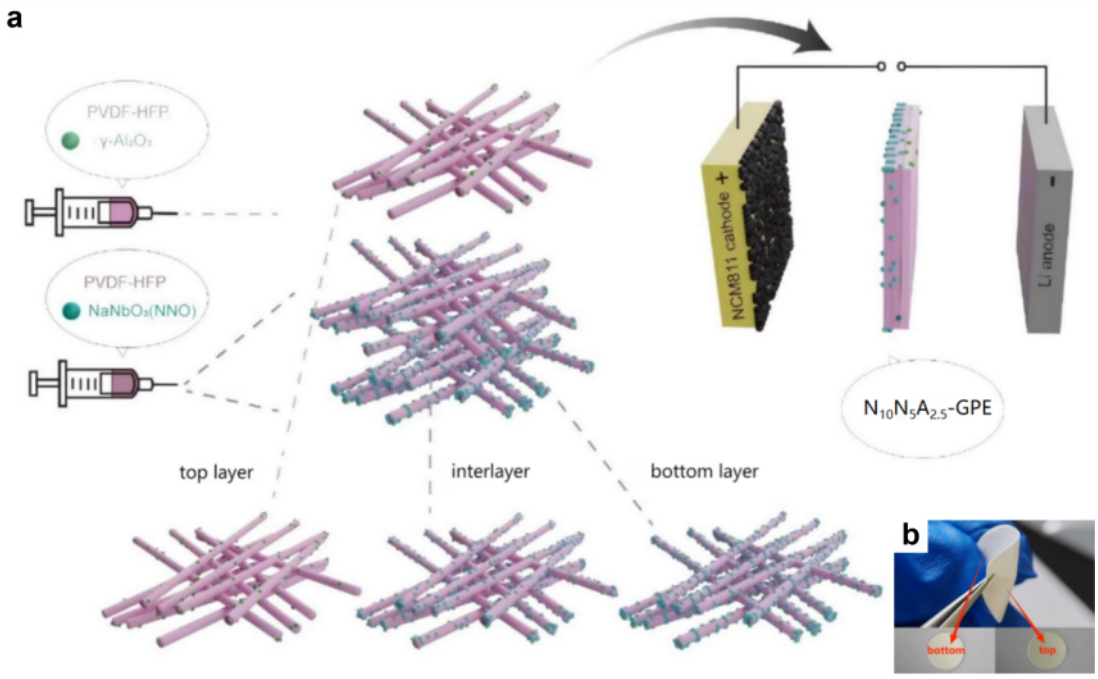

Figure S1. (a) The schematic diagram of the fabrication process for a trilayer asymmetric multifunctional gel polymer electrolyte ($N_{10}N_5A_{2.5}$-GPE); (b) The optical image of the $N_{10}N_5A_{2.5}$-GPE composite membrane.

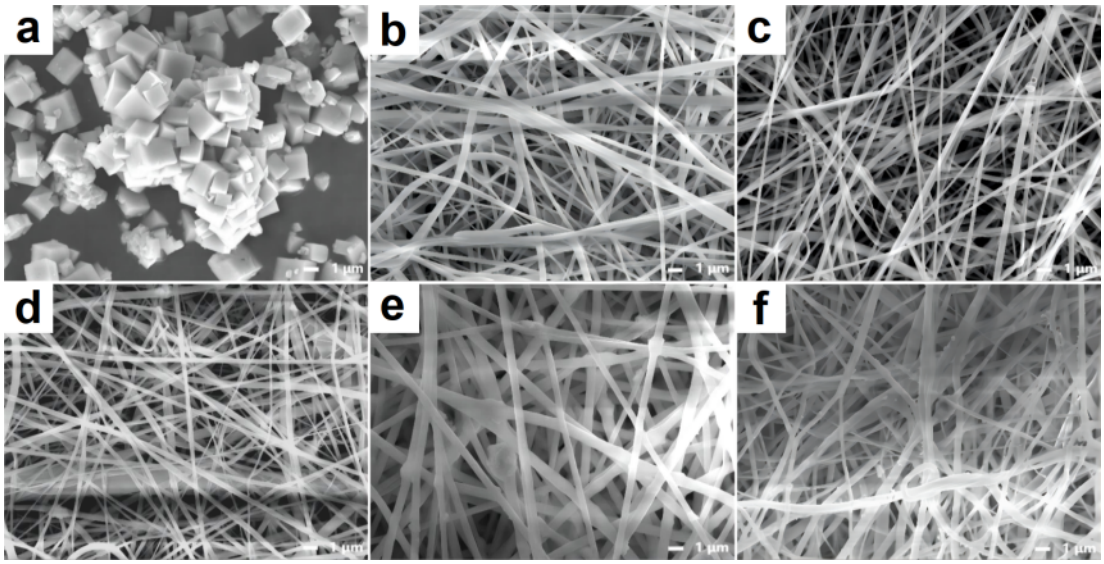

Figure S2. The SEM images of (a) the $NaNbO_3$, (b) pure PVDF-HFP nanofiber membrane and PVDF-HFP nanofiber membranes with different NNO contents: (c) 5 wt%, (d) 10 wt%, (e) 15 wt%, and (f) 20 wt%.

As shown in Figure S2a, the obtained sodium niobate ($NaNbO_3$, NNO) exhibits a cubic nanostructure with a particle size range of approximately 0.5–1.5 μm. As shown in Figure S2b-f, the morphological characteristics of poly(vinylidene fluoride-hexafluoropropylene) (PVDF-HFP) nanofibers with different NNO contents indicate that: When the NNO content does not exceed 10 wt%, the NNO particles can be uniformly dispersed in the PVDF-HFP fiber matrix; when the NNO content is increased to 15 wt%, significant particle agglomeration begins to occur in the system.

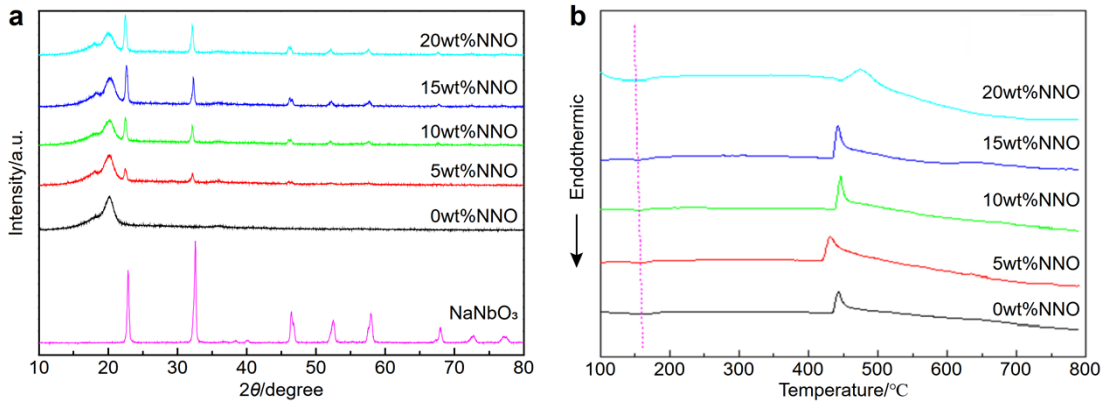

Figure S3. (a) The XRD patterns and (b) DSC spectra.

The crystallization properties of PVDF-HFP polymer membranes with different NNO contents were characterized by X-ray diffraction (XRD) and differential scanning calorimetry (DSC), respectively. The resulting patterns are shown in Figure S3a and b. As shown in Figure S3a, except for the pure PVDF-HFP membrane, all other samples exhibited obvious characteristic peaks of NNO during the XRD test, which proves that NNO is stable to PVDF-HFP.[1] In addition, with the increase of NNO doping amount, the intensity of the characteristic peak also increases significantly. Quantitative analysis shows (Table S1): With the increase of NNO doping amount, the crystallinity of PVDF-HFP shows an obvious downward trend, and this amorphous structure is beneficial to the construction of lithium ion migration channels.[2] Meanwhile, DSC tests (Figure S3b) show that： With the increase of NNO doping amount, the melting temperature of all samples gradually shifts to the low-temperature region, which further confirms that the addition of NNO effectively inhibits the crystallization process of the polymer matrix,[3] and this is consistent with the analysis results of XRD, mutually corroborating each other.

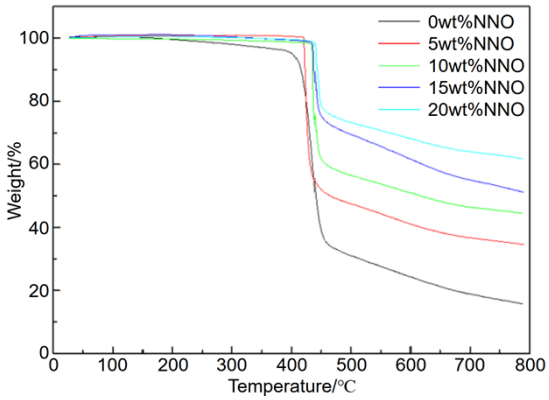

Figure S4. The thermogravimetry curves of PVDF-HFP nanofiber membranes with different NNO contents.

Figure S4 shows the thermogravimetric analysis (TG) curves of PVDF-HFP composite membranes with different NNO doping amounts. The pure PVDF-HFP membrane shows an obvious thermal weight loss platform around 450 °C, which corresponds to the defluorination and decomposition process caused by the breaking of C-F bonds in its main chain.[4] With the gradual addition of NNO, the thermal stability of the composite membrane at high temperatures increases slightly. NNO particles inhibit the thermal movement of polymer segments through interfacial hydrogen bonding, and this improvement in thermal stability plays a crucial role in maintaining the stability of the electrode-electrolyte interface during high-rate charge-discharge processes of lithium-ion batteries.[5]

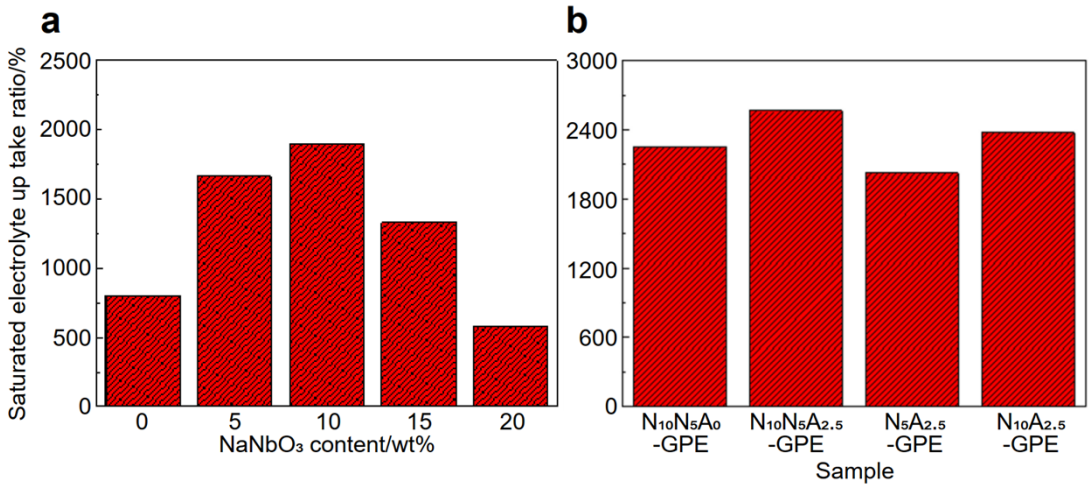

Figure S5. The saturated electrolyte uptake ratios of (a) PVDF-HFP nanofiber membranes with different NNO contents and (b) four multilayer membranes.

Table S2 and Figure S5a, b show the porosity and saturated electrolyte absorption rate of all membrane samples, respectively. There is a significant positive correlation between the two in this experiment, that is, the microporous membranes with high porosity and fully interconnected pore structures exhibit excellent liquid electrolyte adsorption performance. This unique microstructure not only provides effective channels for the rapid penetration of liquid electrolytes but also significantly enhances the conductivity of the membrane by forming a continuous ion transport network. In addition, compared with the single-layer membrane, the saturated electrolyte absorption rates of the four multi-layer membranes are significantly higher. Among them, $N_{10}N_5A_{2.5}$-GPE has the highest saturated electrolyte absorption rate, which also indicates that it may have good ionic conductivity.

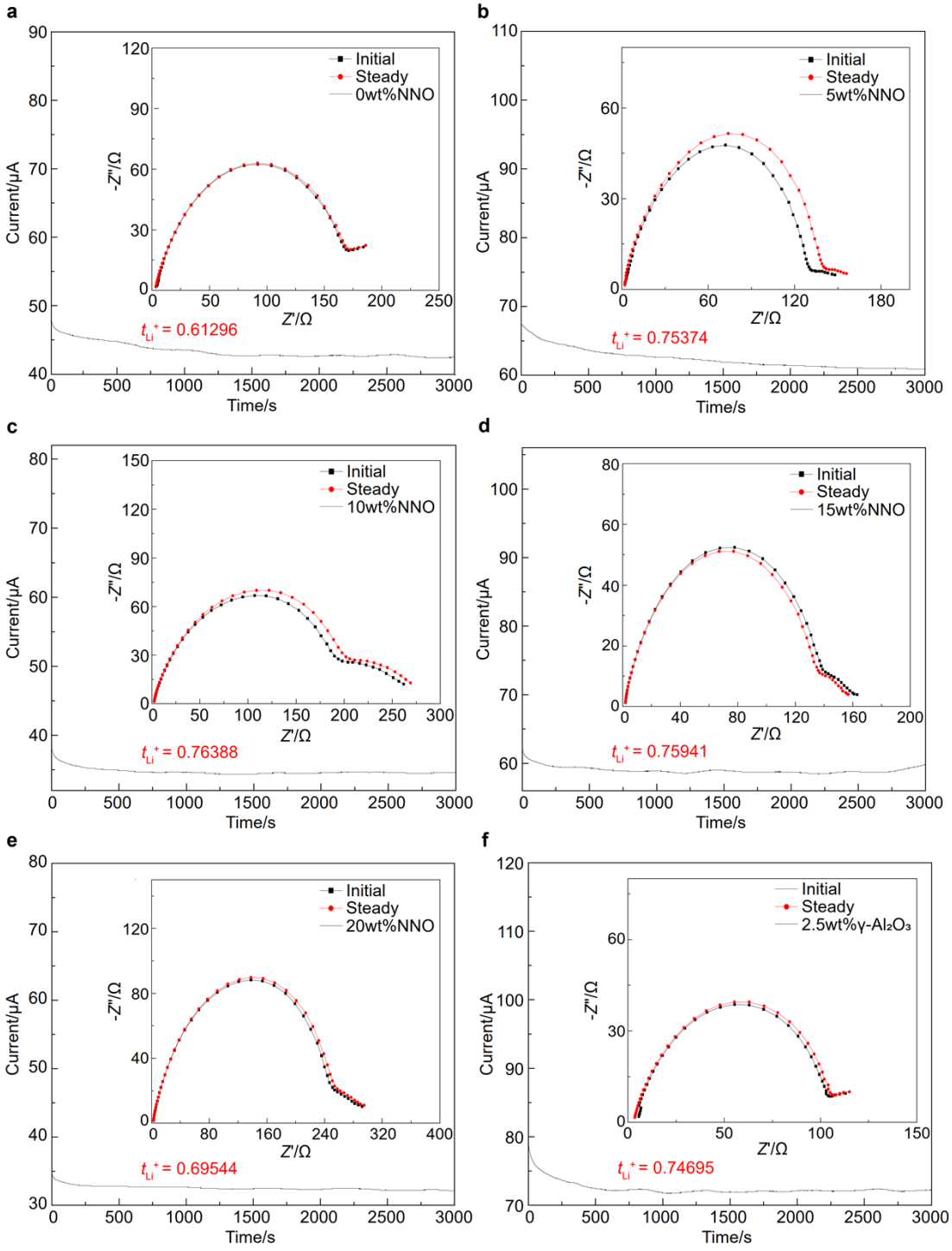
a
Initial
Steady
0wt%NNO
-Z''/Ω
Z'/Ω
Current/μA
Time/s
t_{Li}^+ = 0.61296
b
Initial
Steady
5wt%NNO
t_{Li}^+ = 0.75374
c
Initial
Steady
10wt%NNO
t_{Li}^+ = 0.76388
d
Initial
Steady
15wt%NNO
t_{Li}^+ = 0.75941
e
Initial
Steady
20wt%NNO
t_{Li}^+ = 0.69544
f
Initial
Steady
2.5wt%γ-Al₂O₃
t_{Li}^+ = 0.74695

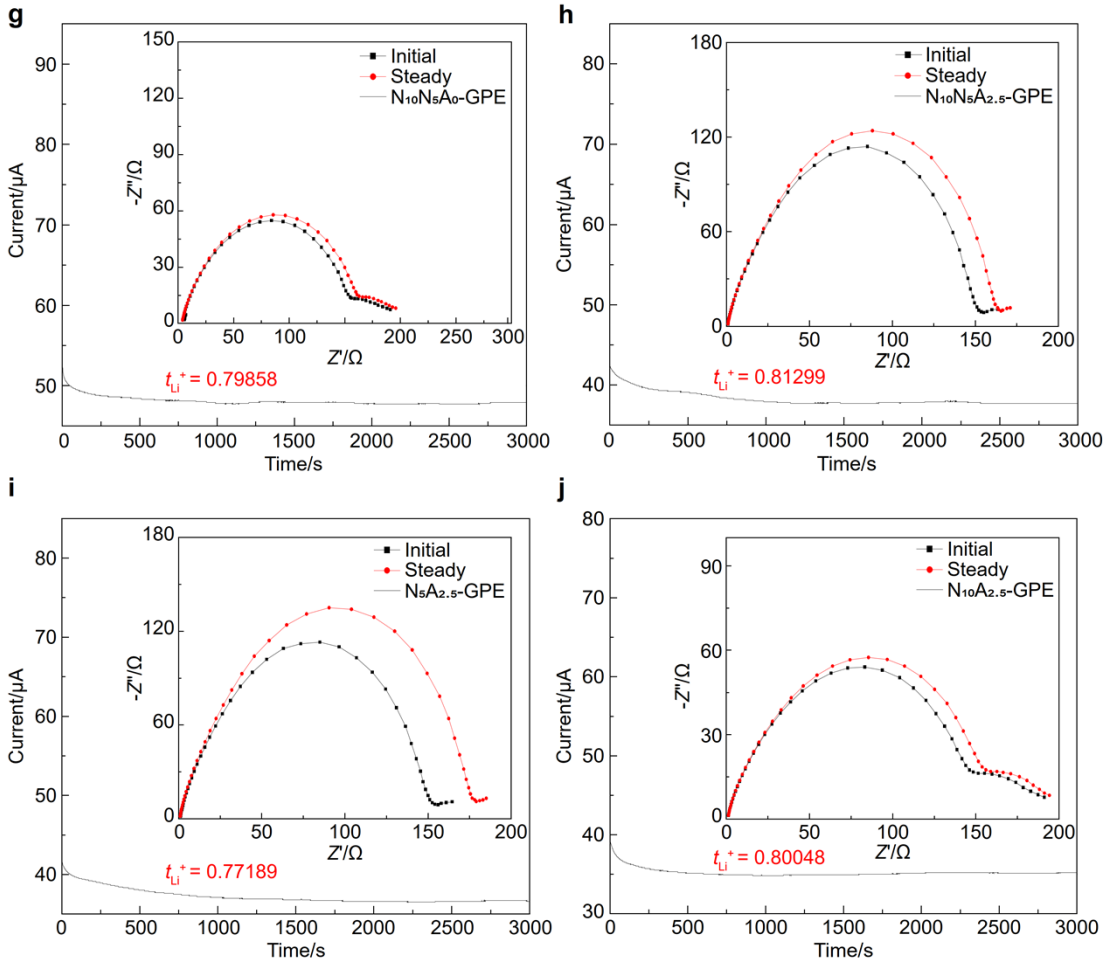

Figure S6. The current-time curves obtained from chronoamperometry of (a) pure PVDF-HFP nanofiber membrane, PVDF-HFP nanofiber membranes with different NNO contents: (b) 5 wt%, (c) 10 wt%, (d) 15 wt%, (e) 20 wt%, (f) the PVDF-HFP nanofiber membrane with 2.5 wt% γ-Al_2O_3 and multilayer membranes: (g) $N_{10}N_5A_0$-GPE, (h) $N_{10}N_5A_{2.5}$-GPE, (i) $N_5A_{2.5}$-GPE, (j) $N_{10}A_{2.5}$-GPE (Impedance spectra of the lithium symmetric cell before and after testing are illustrated in the figure).

In lithium symmetric batteries, the lithium ion transference numbers (t_{Li}^+) of all membrane samples were tested using the chronoamperometry method, and the obtained data are shown in Figure S7a-j. The t_{Li}^+ can be directly calculated from the ratio of the initial current to the steady-state current. GPEs with different contents of NNO all exhibit a high t_{Li}^+ value of around 0.7, and in particular, the GPE with 10 wt% NNO-m added has an extremely high t_{Li}^+ value of up to 0.76388. The high t_{Li}^+ value benefits from the synergistic effect between the polarity of the PVDF-HFP matrix and the high dielectric constant of the NNO filler. This effect optimizes lithium ion transport: on the one hand, it selectively inhibits the migration of macromolecular

PF_6^- anions; on the other hand, it promotes the directional migration of lithium ions, thereby constructing continuous lithium ion transport channels. The optimization of lithium ion transport not only increases the lithium ion transference number but also improves the rate performance of the battery, while inhibiting the growth of overpotential and battery polarization during charge-discharge processes. In the multi-layer membrane system, the t_{Li^+} value of $N_{10}N_5A_{2.5}$-GPE exceeds 0.8, reaching 0.81299, which also indicates its excellent rate performance.

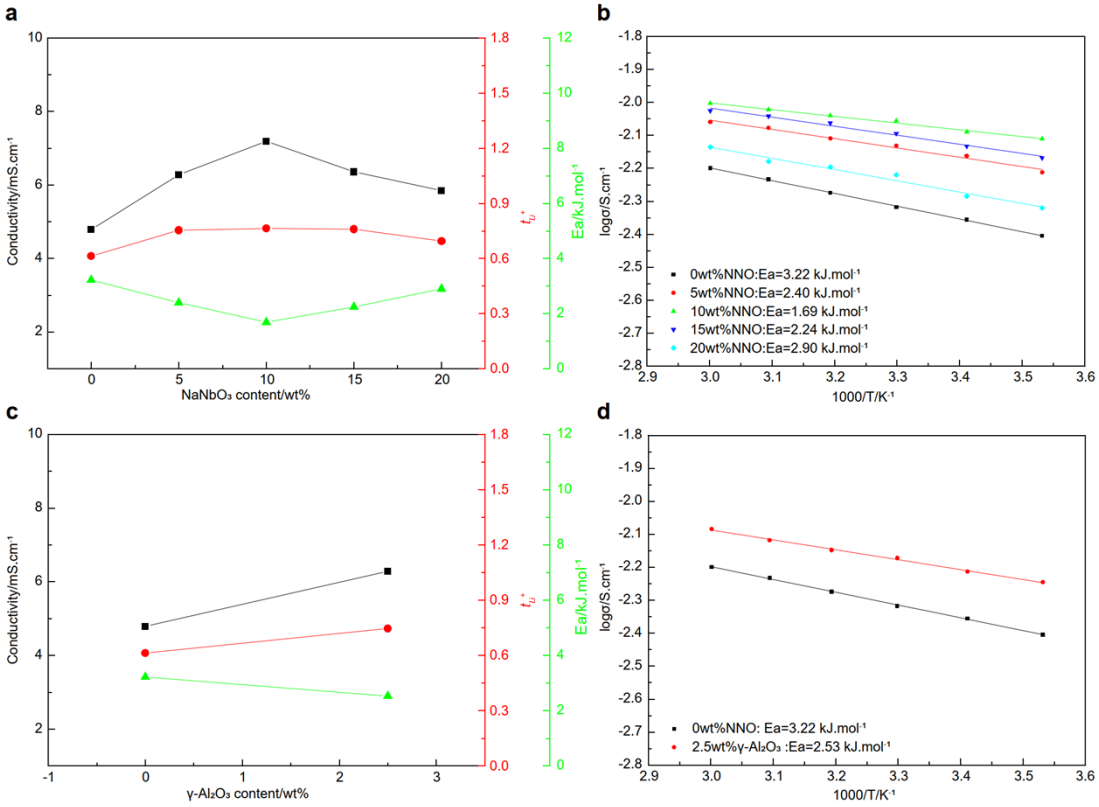

Figure S7. The ionic conductivity, lithium ion transference number (t_{Li}^+) at room temperature and activation energy (E_a) of PVDF-HFP nanofiber membranes with different (a) NNO and (c) γ-Al_2O_3 contents; The temperature-dependent ionic conductivity plots of PVDF-HFP nanofiber membranes with different (b) NNO and (d) γ-Al_2O_3 contents.

Figure S7a shows the ion conductivity and lithium ion migration number $t_{Li}^+$of GPE corresponding to PVDF-HFP membranes with different contents of NNO added. It can be seen that with the gradual increase of NNO content, the room temperature ionic conductivity and t_{Li}^+value of corresponding GPE show a trend of first increasing and then decreasing, reaching peak points of 7.19 mS cm^{-1} and 0.76388 at NNO content of 10 wt%. According to the Arrhenius curve (Figure S7b), the corresponding activation energy E_a was calculated, and it was found that as the NNO content gradually increased, the E_a value showed a trend of first decreasing and then increasing. Figure S7c shows the ion conductivity and lithium ion migration number t_{Li}^+ of GPE corresponding to PVDF-HFP membrane before and after the addition of 2.5 wt% γ-Al_2O_3. It can be seen that the addition of γ-Al_2O_3 significantly improved the ion conductivity and t_{Li}^+ value, reaching 6.09 mS.cm^{-1} and 0.74695, respectively. As the testing temperature increases, their ionic conductivity also increases. According to the Arrhenius curve (Figure S7d), the corresponding activation energy Ea was calculated, and it

was found that compared to the pure PVDF-HFP membrane, the addition of γ-Al_2O_3 also significantly reduced the Ea value.

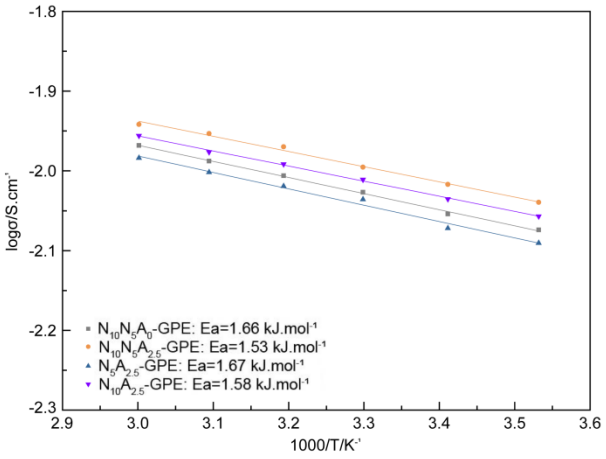

Figure S8. The temperature-dependent ionic conductivity plots of four multilayer membranes.

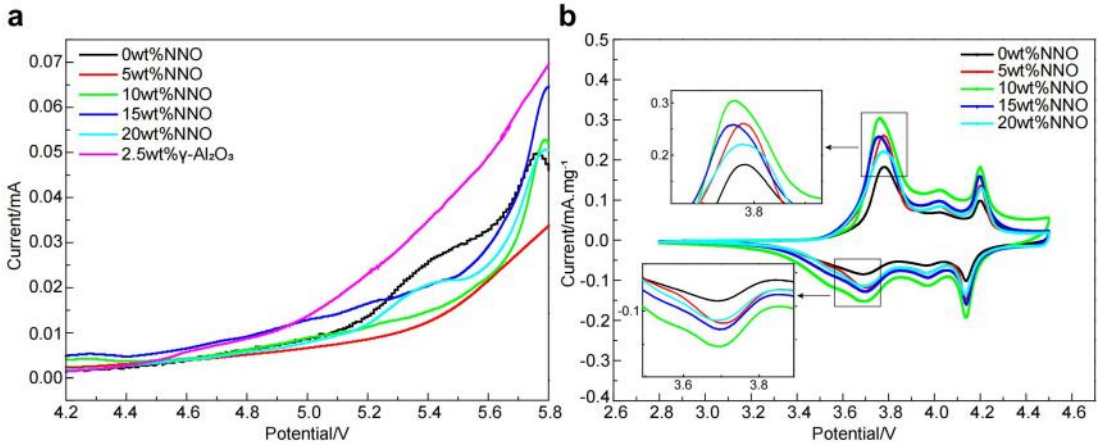

Figure S9. (a) The linear sweep voltammetry curves of all single-layer membranes obtained from Li/GPE/SS cells; (b) The cyclic voltammetry curves of PVDF-HFP nanofiber membranes with different NNO contents obtained from NCM811/GPE/Li cells.

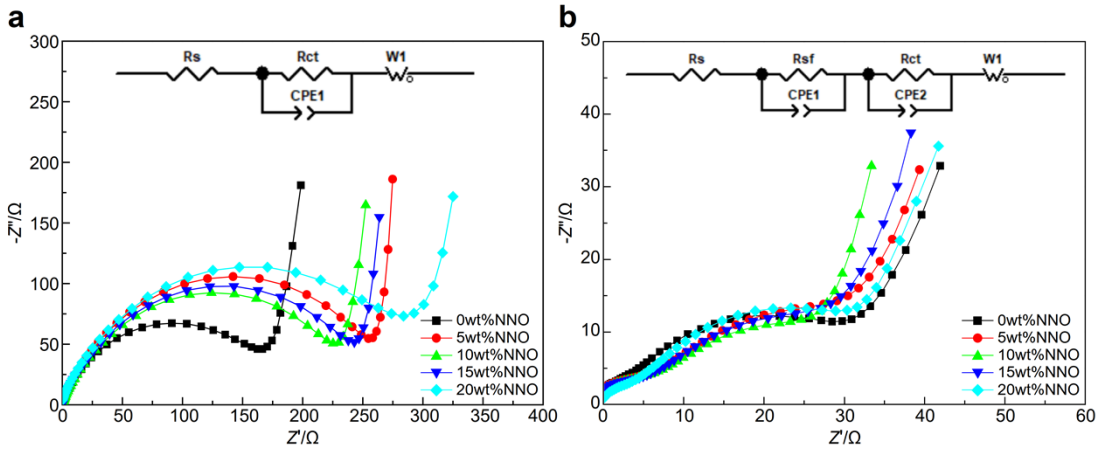

Figure S10. The electrochemical impedance spectroscopies of PVDF-HFP nanofiber membranes with different NNO contents (a) before and (b) after 150 cycles obtained from NCM811/GPE/Li cells.

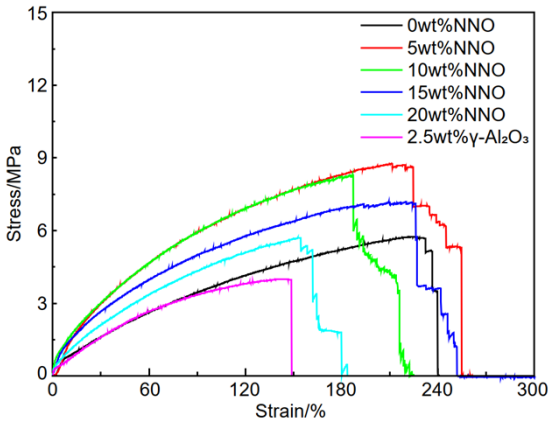

Figure S11. The stress-strain curves of all single-layer membranes.

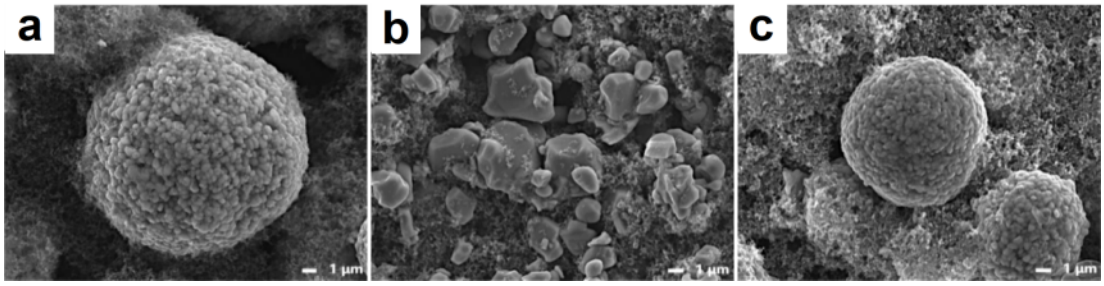

Figure S12. The SEM images of (a) the pristine NCM811 cathode and NCM811 cathodes after 150 cycles obtained from (b) NCM811/0 wt% NNO/Li, (c) NCM811/$N_{10}N_5A_{2.5}$-GPE/Li cells at 5000x magnification.

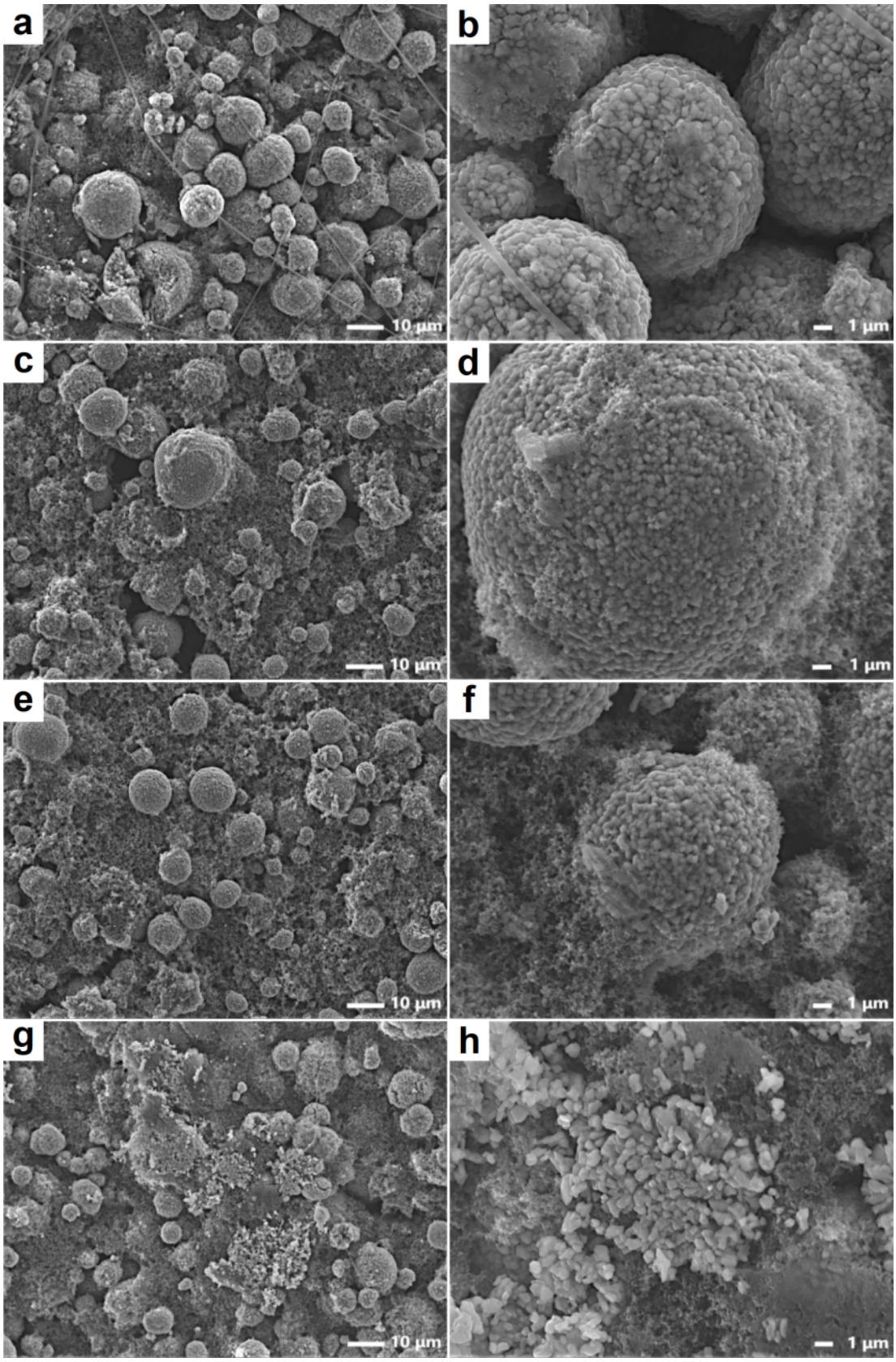

Figure S13. The SEM images of NCM811 cathodes after 150 cycles obtained from (a, b) NCM811/5 wt% NNO/Li, (c, d) NCM811/10 wt% NNO/Li, (e, f) NCM811/15 wt% NNO/Li and (g, h) NCM811/20 wt% NNO/Li cells at 1000x (left) and 5000x m

agnification (right).

Figure S13 shows the surface morphology of NCM811/GPE/Li battery assembled based on different NNO content GPE after 150 cycles at 1 C, obtained by disassembling the NCM811 electrode (taken at 1000 times on the left and 5000 times on the right). At low magnification, it can be observed that a low (5 wt%) or high (20 wt%) NNO content can cause significant spherical particle breakage or agglomeration (Figure S13a and g), which seriously affects the uniform diffusion of Li^+ in the electrode under high voltage, exacerbates interface side reactions, and leads to deterioration of cell rate performance and cycling stability. In contrast, when the NNO content is 10 wt% and 15 wt%, the spherical structure is relatively intact, without obvious microcracks or particle aggregation (Figure S13c and e). Upon further observation at high magnification, it can be observed that when the NNO content is 10 wt%, the secondary particles are more tightly bound, resulting in fewer surface by-products and a more uniform CEI film (Figure S13b, d, f, and h). This helps to reduce interfacial impedance, minimize side reactions, and improve the electrochemical performance and thermal stability of the battery.

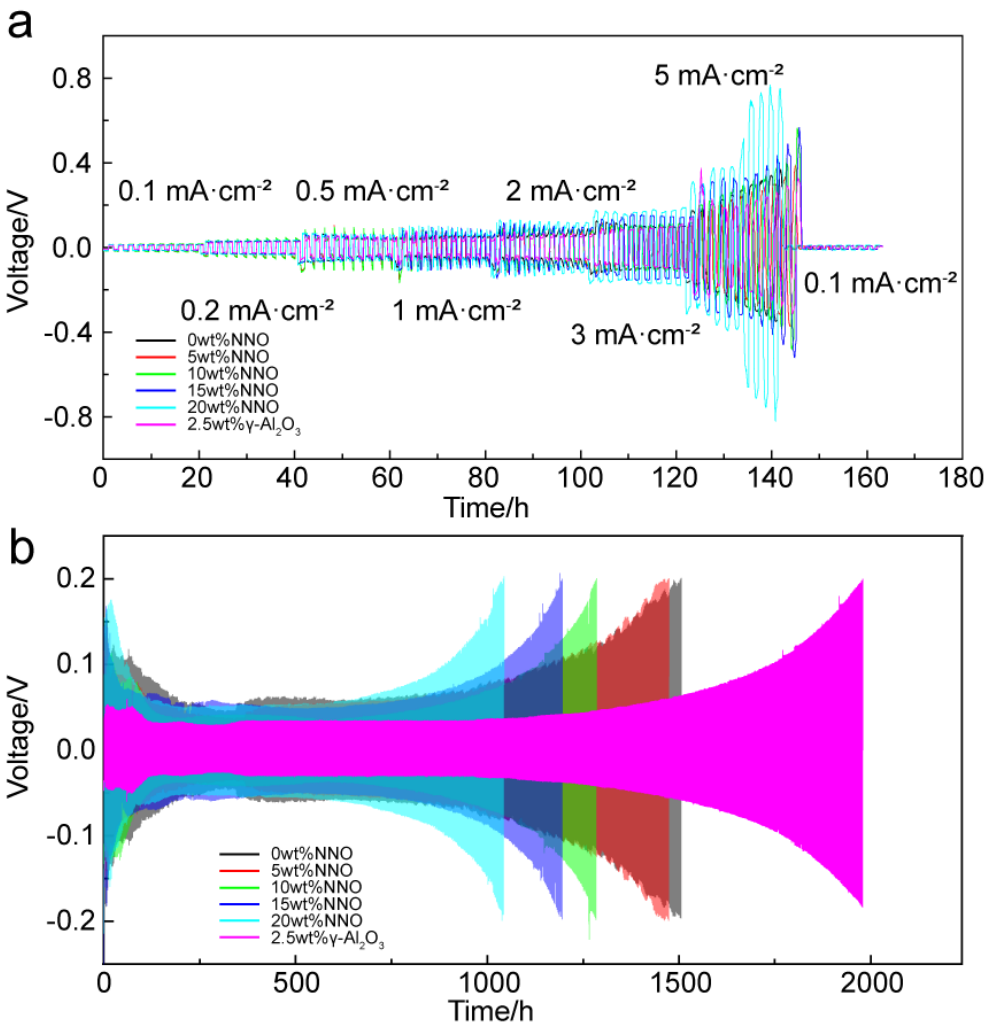

Figure S14. The voltage-time curves of all single-layer membranes in lithium symmetric cells (a) under different current densities and (b) at a current density of 0.5 mA cm^{-2}.

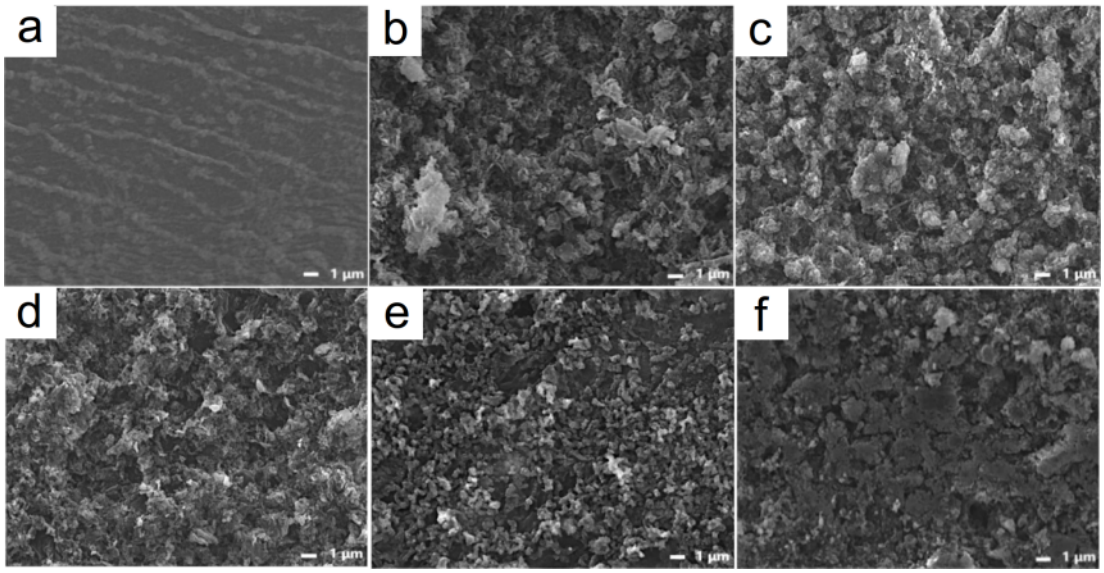

Figure S15. The SEM images of (a) the pristine Li anode and Li anodes after lithium plating/stripping cycled for 300 h obtained from (b) Li/5 wt% NNO/Li, (c) Li/10 wt% NNO/Li, (d) Li/15 wt% NNO/Li, (e) Li/20 wt% NNO/Li and (f) Li/2.5 wt% γ-Al_2O_3/Li cells at 5000x magnification.

Figure S15a-f show the surface morphology of lithium sheets obtained by disassembling Li/GPE/Li batteries assembled based on GPE with different NNO contents before and after continuous charging and discharging for 300 hours at a current density of 0.5 mA cm^{-2} (taken at 5000 times magnification). It can be seen that with the gradual increase of NNO content, the block like structure on the surface of the lithium sheet gradually increases. When the NNO content is 5 wt%, the granular structure and block structure are mixed together (Figure S15b); When the NNO content is 10 wt%, almost all of them have block like structures (Figure S15c); As the NNO content further increases, the blocky structure begins to break, forming a large number of pores. Both block like structures and pores accelerate the consumption of electrolyte, leading to interface instability. In addition, with the gradual increase of NNO content, the uniformity of particle distribution on the surface of lithium sheets gradually decreases. When the NNO content is 15 wt%, there is slight particle detachment in the upper right corner area (Figure S15d); When the NNO content is 20 wt%, a large area of particle detachment appears in the upper right corner region (Figure S15e). The detachment of particles on the surface of lithium sheets not only causes the accumulation of dead lithium, but also makes the surface of the lithium sheet uneven, forming a porous structure inside, thereby exacerbating side reactions, deteriorating the anode electrolyte interface, and making

it easier to form lithium dendrites, resulting in structural collapse. When the content of γ-Al_2O_3 is 2.5 wt%, the surface roughness of the lithium sheet is significantly reduced, the boundaries of the particles are clearer, and the size is more uniform (Figure S15f).

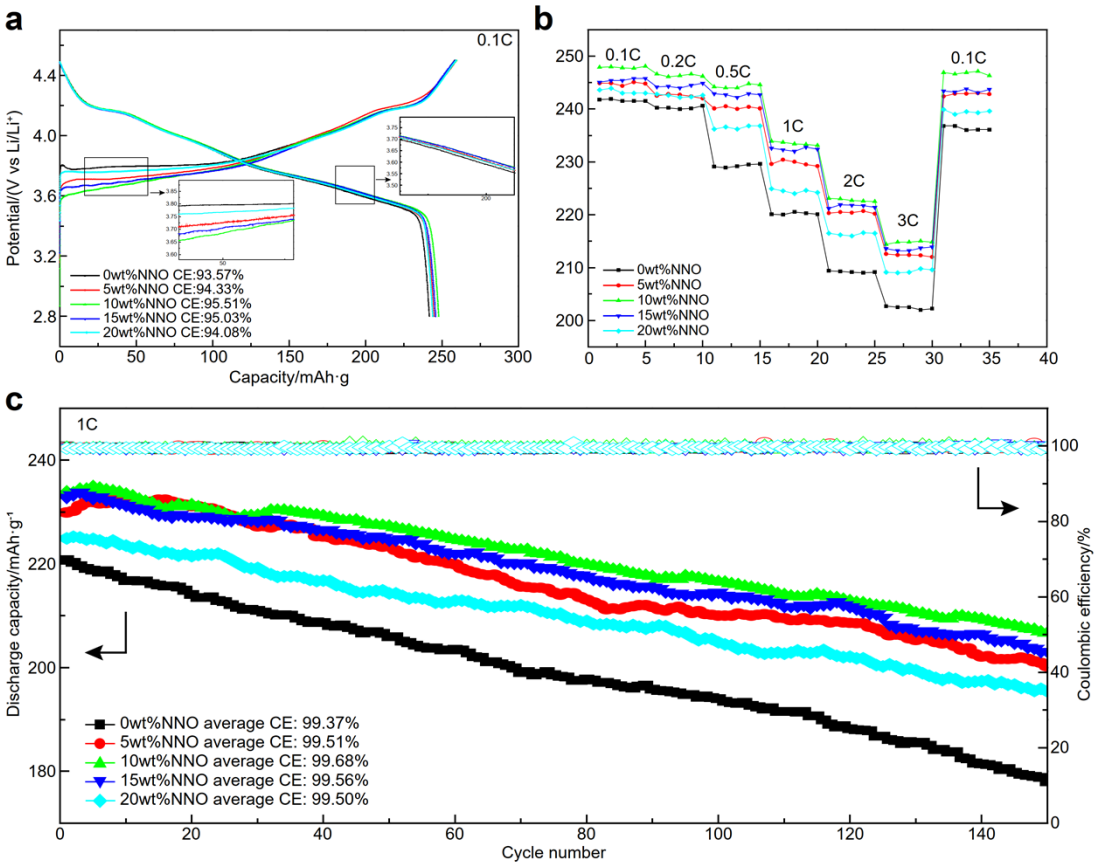

Figure S16. (a) The first-cycle charge/discharge curves of PVDF-HFP nanofiber membranes with different NNO contents obtained from NCM811/GPE/Li cells with 4.5 V cut-off at 0.1 C at 25 ℃; (b) The rate performance curves of PVDF-HFP nanofiber membranes with different NNO contents obtained from NCM811/GPE/Li cells with 4.5 V cut-off at 25 ℃; (c) The cycle performance curves of PVDF-HFP nanofiber membranes with different NNO contents obtained from NCM811/GPE/Li cells with 4.5 V cut-off at 1 C at 25 ℃.

Table S1. The heat enthalpy of the melting (ΔH_m) and crystalline degree (X_c) of all membrane samples

Membrane	0wt% NNO	5wt% NNO	10wt% NNO	15wt% NNO	20wt% NNO
ΔH_m/J g^{-1}	22.65	15.16	13.13	11.69	10.23
X_c/%	21.63	15.20	13.79	12.84	11.72

Table S2. The porosity of all membrane samples

Sample	0wt% NNO	5wt% NNO	10wt% NNO	15wt% NNO	20wt% NNO	$N_{10}N_5A_0$-GPE	$N_{10}N_5A_{2.5}$-GPE	$N_5A_{2.5}$-GPE	$N_{10}A_{2.5}$-GPE
Porosity/%	67.5	82.7	85.9	78.1	50.6	88.3	91.1	86.5	89.8

Table S3. The comparison of ionic conductivity, test conditions and capacity retention of electrolyte materials with previous similar reports

Electrolyte material	Ionic conductivity/mS.cm^{-1}	Test condition	Capacity retention	Reference
PVDF-HFP/$BaTiO_3$	5.20	2.5-4.5 V 5 C 200 cycles	70%	[3]
PVDF-HFP/YSZ	1.01	3.0-4.5 V 1 C 400 cycles	70.13%	[6]
PVDF-HFP/TiO_2	1.68	2.5-4.5 V 1 C 500 cycles	72%	[7]
PVDF-HFP/CAP	1.30	3.0-4.4 V 0.5 C 100 cycles	77%	[8]
PVDF-HFP/titania-PMMA	3.40	2.75-4.4 V 0.5 C 100 cycles	87.06%	[9]
PVDF-HFP/$NaNbO_3$ & γ-Al_2O_3	8.09	2.8-4.5 V 5 C 1000 cycles	66.22%	This work

References

1. S. Huo, L. Sheng, W. Xue, L. Wang, H. Xu, H. Zhang, and X. He, *InfoMat*, 2023, **5**, e12394.
2. J. Ding, D. Ji, Y. Yue, and M. M. Smedskjaer, *Small*, 2024, **20**, 2304270.
3. M. Zhu, J. Wu, B. Liu, W. H. Zhong, J. Lan, X. Yang, and G. Sui, *Journal of Membrane Science*, 2019, **588**, 117194.
4. J. C. Dias, D. M. Correia, C. M. Costa, G. Botelho, J. L. Vilas-Vilela, and S. Lanceros-Méndez, *Polymer*, 2021, **229**, 123995.
5. N. Mehra, L. Mu, and J. Zhu, *Composites Science and Technology*, 2017, **148**, 97–105.
6. W. Yuan, J. Liao, S. Huang, D. Song, Q. Su, C. Li, and J. He, *Journal of Energy Storage*, 2025, **106**, 114618.
7. M. R. Asghar, M. T. Anwar, G. Xia, and J. Zhang, *Materials Chemistry and Physics*, 2020, **252**.
8. F. Chen, Y. Liao, M. Li, J. Huang, Q. Huang, and W. Li, *Journal of The Electrochemical Society*, 2018, **165**, A206.
9. J. Cao, L. Wang, M. Fang, X. He, J. Li, J. Gao, L. Deng, J. Wang, and H. Chen, *Journal of Power Sources*, 2014, **246**, 499–504.